

A EUROPEAN JOURNAL

CHEMPHYSICHEM

OF CHEMICAL PHYSICS AND PHYSICAL CHEMISTRY

Accepted Article

Title: Mixed-Metal Tungsten Oxide Photoanode Materials Made by Pulsed-Laser in Liquids Synthesis

Authors: Carl M Blumenfeld, Marcus Lau, Harry B Gray, and Astrid M Müller

This manuscript has been accepted after peer review and appears as an Accepted Article online prior to editing, proofing, and formal publication of the final Version of Record (VoR). This work is currently citable by using the Digital Object Identifier (DOI) given below. The VoR will be published online in Early View as soon as possible and may be different to this Accepted Article as a result of editing. Readers should obtain the VoR from the journal website shown below when it is published to ensure accuracy of information. The authors are responsible for the content of this Accepted Article.

To be cited as: *ChemPhysChem* 10.1002/cphc.201601285

Link to VoR: <http://dx.doi.org/10.1002/cphc.201601285>

WILEY-VCH

www.chemphyschem.org

A Journal of



Mixed-Metal Tungsten Oxide Photoanode Materials Made by Pulsed-Laser in Liquids Synthesis

Carl M. Blumenfeld,^[a] Marcus Lau,^[b] Harry B. Gray,^[a] and Astrid M. Müller*^[a]

Abstract: Globally scalable sunlight-driven devices that convert solar energy into storable fuels will require efficient light absorbers that are made of non-precious elements. Suitable photoanode materials are yet to be discovered. Here we utilised the timesaving nature of pulsed-laser in liquids synthesis and prepared a series of neat and mixed-metal tungsten oxide photoanode materials to investigate the effect of ad-metals on optical and photocurrent generation properties. We obtained sub- μm -sized materials with different colours from W, Al, Ta, or first-row transition metal targets in water or aqueous ammonium metatungstate solutions. We observed metastable polymorphs of WO_3 and tungsten oxides with varying degrees of oxygen deficiency. Pulsed-laser in liquids synthesis of Ni in ammonium metatungstate solutions produced hollow spheres (with $\leq 6\%$ Ni with respect to W). Photocurrent generation in strong aqueous acid was highest in mixed-metal tungsten oxide photoanode materials with around 5% of iron or nickel.

Introduction

Conversion of solar energy into renewable, storable fuels is essential to meet future global energy demands.^[1] Devices for sunlight-driven water splitting or artificial photosynthesis must consist of materials that are made of non-precious elements to enable worldwide scalability.^[2] Photoelectrochemical (tandem) devices offer advantages because the processes of light capture and catalysis are decoupled, and the anodic and cathodic components and half reactions are separated.^[3] While great strides have been made with Si ,^[4] InP ,^[5] or WSe_2 ,^[6] photocathodes, suitable photoanode materials are yet to be discovered.

Good photoelectrodes are efficient light absorbers and charge carrier transporters.^[7] Semiconductor photoanodes must also have a valence band edge that is positive enough for the generation of overpotentials sufficient to drive water oxidation,^[8] a flatband potential that enables early water-oxidation onset,^[3b]

and they should have a bandgap of 1.95 eV, to make the best use of sunlight in a tandem water-splitting device.^[9]

Tungsten trioxide, WO_3 , is a promising earth-abundant photoanode material.^[10] But the high bandgap of its thermodynamically most stable γ -monoclinic phase of 2.6 eV^[11] limits the efficient absorption of sunlight. Much effort has been spent on shifting the optical bandgap into the visible range for optimised light capture while simultaneously avoiding deep traps at which charge carriers recombine.^[12] The intercalation of molecular nitrogen into the WO_3 lattice has been shown to reduce the bandgap to 1.9 eV; nevertheless, stable photocurrents were only moderately enhanced.^[13] A recent report showed that a thin tungsten oxide overlayer with dual oxygen and tungsten vacancies on mesoporous WO_3 photoanodes improved photocurrents by a factor of 2.4 due to better interfacial charge transfer and conductivity.^[14]

Tungsten oxide has been extensively studied theoretically. In work of note, Ping and Galli computed the bandgaps of γ -monoclinic WO_3 and phases that were stable at high temperature or under pressure; they found that relative positions of the WO_6 units in the unit cells and W–O–W angles, which differed among the crystal phases, led to changes in electronic and optical properties. For example, orthorhombic WO_3 had a smaller bandgap and improved electron and hole mobilities compared to the thermodynamically most stable monoclinic crystal phase; the bandgaps of tetragonal and cubic WO_3 were below 2 eV, shifting their absorptions into the visible range and thus making them more efficient sunlight absorbers.^[15] Pham, Ping, and Galli recently reviewed the design criteria for heterogeneous interfaces for solar water splitting by modelling photoelectrode–water interfaces. They established that band edge positions of photoelectrode materials were strongly dependent on the structure and chemistry of the aqueous interface. Detailed understanding of solvation, especially for hydrophilic surfaces with surface defects such as O vacancies at WO_3 surfaces, is of key importance.^[16] Gerosa et al. used first-principles calculations to shed light on how structurally inequivalent oxygen vacancies affected charge recombination and optical properties in oxygen-deficient tungsten oxide.^[17]

We prepared mixed-metal tungsten oxide photoanode nanomaterials by pulsed-laser in liquids synthesis to investigate the effect of ad-metals on optical and photocurrent generation properties. Since Fojtik and Henglein first demonstrated pulsed-laser in liquids syntheses of gold, nickel, and carbon colloids,^[18] numerous metal, alloy, oxide, semiconductor, ceramics, and carbon nanoparticles have been made with the technique.^[19] Laser-made tungsten oxides have also been reported. Li and Cai et al. prepared WO_3 nanomaterials by infrared pulsed laser in liquids syntheses; they obtained leaf-like or cuboidal morphologies from colloidal precursor solutions by ageing at

[a] C. M. Blumenfeld, Prof. H. B. Gray, Dr. A. M. Müller
Beckman Institute, Division of Chemistry and Chemical Engineering
California Institute of Technology
1200 E California Blvd., Mail Code 139-74, Pasadena, CA 91125,
USA

E-mail: astridm@caltech.edu

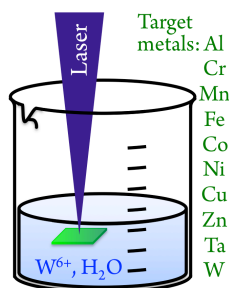
[b] Dr. M. Lau
Permanent address:
Technical Chemistry I, University of Duisburg-Essen
Universitätsstrasse 7, 45141 Essen, Germany

Supporting information for this article is given via a link at the end of the document.

room temperature^[20] or a subsequent hydrothermal route.^[21] Recently, infrared-laser-synthesised electrochromic tungsten oxide hydrate films have been reported.^[22]

We developed pulsed-laser in liquids synthesis protocols, using 10 Hz repetition rate, 8 ns, 355 nm pulses. The biggest advantages of the technique are its vast number of tuneable variables (chemical nature of precursors and liquid, laser parameters etc.), the unnecessary of surfactants, and the fast synthesis timescale. We utilised our experimental design as a synthetic tool to rapidly optimise novel multi-metal nanomaterials with advanced functionalities, such as highly active Co_3O_4 ^[23] and nickel-iron layered double hydroxide^[24] water oxidation catalysts. We established that nickel-iron-based nanosheets with two additional Lewis-acidic metal ions outperformed neat nickel-iron-based catalysts,^[24a] and addition of appropriate anions to the liquid predictably produced complex phase-pure Cu and Zn based nanominerals.^[25] The technique of this work likely encompasses all three regimes of pulsed-laser in liquids synthesis (ablation, fragmentation, and melting). Irrespective of the exact mechanism of nanoparticle formation, our approach is a useful tool to rapidly prepare novel nanomaterials that contain multiple metals.

We prepared fourteen tungsten-oxide-based materials by pulsed-laser synthesis from metal targets in water or aqueous ammonium metatungstate solutions (Scheme 1).



Scheme 1. Schematic illustration of targets and liquids of the pulsed-laser syntheses of this work.

We used earth-abundant first-row transition metals, aluminium, or tantalum as ad-metals. Heterogeneous water oxidation catalysts made solely of non-precious elements have higher activities if high-valent metal-oxo centres that are accessible at moderate anodic potentials can be formed.^[1] This is why we chose Cr, Mn, Fe, and Co precursors. It has also been shown that addition of redox-inert metals, such as Al or Zn, promotes water oxidation activity.^[26] Oxygen evolution catalysts based on Ni and Cu have been reported,^[1] and tantalum (hydr)oxides do not corrode in aqueous acid, even at high anodic bias.^[27] For comparison, we also synthesised neat tungsten oxide materials. We determined the elemental compositions of our materials by energy-dispersive X-ray spectroscopy (EDX), assessed the oxidation states of the ad-metals by X-ray photoelectron spectroscopy (XPS), obtained crystalline phases by X-ray

diffraction (XRD), and acquired scanning electron microscopy (SEM) images to visualise nanoparticle shapes and sizes.

We assessed our laser-synthesised nanoparticles on fluorine-doped tin oxide coated glass supporting electrodes in strongly acidic aqueous electrolyte and illuminated the resulting photoanodes with simulated sunlight from the front side, as required for practical use in integrated water-splitting or artificial photosynthesis devices.

Results and Discussion

Our laser-made tungsten-oxide-based nanomaterials exhibited different colours (Figure 1). We used metal foil or powder targets in neat water or aqueous solutions of ammonium metatungstate. In accordance with previous reports,^[19k, 25, 28] nanoparticle yields were higher with powder targets because of their larger surface area compared to metal foils.

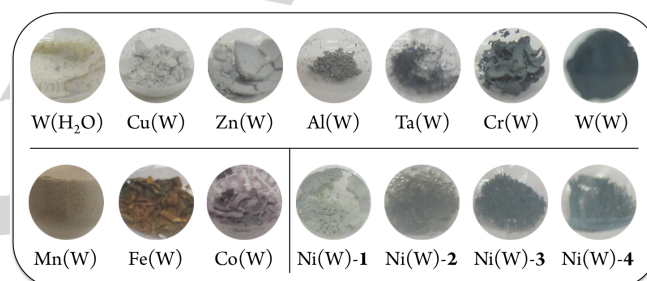


Figure 1. Photos of laser-synthesised tungsten-based materials; see Table 1 for nomenclature.

We determined the relative proportions of ad-metals with respect to tungsten in our mixed-metal materials by energy-dispersive X-ray (EDX) spectroscopy (Table 1 and Figure 2).

Table 1. Pulsed-laser-synthesised tungsten-based materials, target metals liquid compositions, and relative proportions of ad-metals with respect to tungsten, the relative error is at most 7%.

Material ^[a]	Target	Liquid ^[b]	wt% M ^[c]
Al(W)	Al foil	3.0 g AMT	9.0 (Al)
Cr(W)	2.0 g Cr powder	3.0 g AMT	1.1 (Cr) 3.9 (Fe)
Mn(W)	0.75 g Mn powder	3.0 g AMT	41.2 (Mn)
Fe(W)	1.0 g Fe powder	5.0 g AMT	83.7 (Fe)
Co(W)	1.0 g Co powder	5.0 g AMT	18.2 (Co)
Ni(W)-1	2.5 g Ni powder	3.0 g AMT	14.3 (Ni)
Ni(W)-2	1.8 g Ni powder	3.0 g AMT	6.1 (Ni)
Ni(W)-3	0.9 g Ni powder	3.0 g AMT	3.1 (Ni)

Ni(W)-4	0.9 g Ni powder	4.0 g AMT	2.8 (Ni)
Cu(W)	Cu foil	3.0 g AMT	2.0 (Cu) 8.6 (Al)
Zn(W)	Zn foil	3.0 g AMT	21.3 (Zn)
Ta(W)	Ta foil	5.0 g AMT	9.4 (Ta)
W(W)	2.0 g W powder	3.0 g AMT	–
W(H ₂ O)	2.0 g W powder	H ₂ O	–

[a] First element, target; in parentheses, liquid (neat water or aqueous tungsten salt solution, see Experimental Part for details). [b] AMT (ammonium metatungstate hydrate) dissolved in 10 mL water. [c] Relative proportion of ad-metal M (in parentheses) with respect to tungsten content, from EDX data.

We acquired EDX spectra at three spots on the electron image and found similar compositions, indicating uniform distributions of elements throughout the materials. All EDX spectra showed contributions that were attributable to Si, stemming from the electron microscopy substrates. We did not quantify oxygen or carbon contents because O and C also occur in adventitious sources or are attributable to the substrate, such as SiO₂. Importantly, we did not detect any nitrogen in the EDX or XPS spectra, indicating that no ammonium metatungstate (AMT) precursor was left in the synthesised materials.

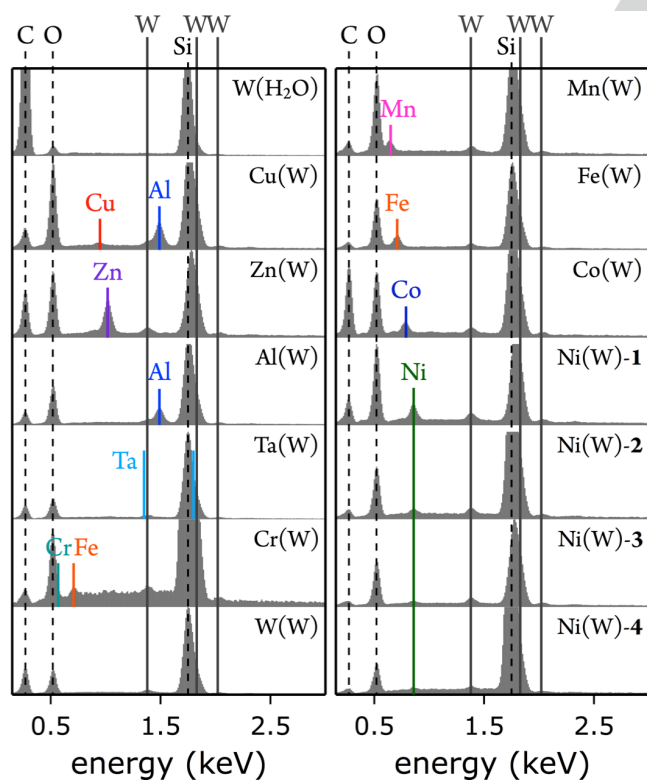


Figure 2. EDX spectra of laser-synthesised materials; see Table 1 for nomenclature and element quantification. The elements C, O, and Si (dashed lines) are adventitious or from the substrate; solid lines indicate other elements.

Pulsed-laser synthesis of tungsten in water or aqueous AMT^[29] solution resulted in materials that did not contain any ad-metals. Tungsten targets (powder or foil) in neat water produced a light yellow solid. X-ray diffraction (XRD) data are consistent with metallic W and cubic WO₃ (Figure S1). Tungsten in aqueous AMT solution led to a deep blue solid (Figure 1). Its XRD pattern (Figure S1) suggested it contained, in addition to metallic W and orthorhombic WO₃, an oxygen-deficient tungsten oxide (monoclinic WO_{2.92}), giving rise to the deep blue colour.

Oxygen-deficient tungsten oxides are also called tungsten blue oxides because of their deep blue colouration. Ammonium tungstate easily converts into tungsten blue oxides with variable degrees of oxygen deficiency, depending on calcination parameters, such as temperature (typically 300–900°C), heating time (typically several hours), and composition and pressure of the reducing atmosphere.^[30] Tungsten blue oxide is an important industrial intermediate with grain sizes on the order of ten to a hundred μm for reduction to tungsten powder and non-sag metal.^[31] Oxygen-deficient tungsten oxide nanoparticles are harder to obtain, although a synthesis in supercritical fluids was recently reported.^[32] Our facile pulsed-laser synthesis in aqueous AMT solution offers advantages because its many tuneable parameters provide the synthetic flexibility needed to access many different materials, compositions, and polymorphs.

Materials prepared from Al, Mn, Fe, Co, Ni, Zn, or Ta targets exhibited peaks for tungsten and the respective target metals in the EDX spectra, whereas materials synthesised from Cu or Cr targets contained two ad-metals: Cu and Al for copper foil, and Cr and Fe for chromium powder. Our copper foil had only commercial purity (>95%) and was alloyed with (0.4 ± 0.2) wt% aluminium to impart higher strength while retaining electrical conductivity, as evidenced by inductively coupled plasma mass spectrometry (ICP-MS) data. The chromium powder had a purity of 99.7%, making it an unlikely source of Fe. It has been shown in the context of Ni(OH)₂ syntheses that incidental iron incorporation is common when regular glassware is used.^[33] Therefore, we assume that the small amount of iron we detected in the material synthesised from Cr powder in aqueous AMT solution stems from ubiquitous sources.

We observed that materials synthesised from W in water, Cu, Zn, Al, Ta, Cr, or W in aqueous AMT solutions exhibited colours that steadily changed from white to blue (Figure 1). The Cu-based material was X-ray amorphous. XRD data of the other materials (Figure S1) showed that the crystalline phases could be assigned to ad-metal phases, mixed ad-metal tungsten phases, or tungsten blue oxides. Zn(W) contained crystalline monoclinic WO₃ and the oxygen-deficient zinc tungsten oxide Zn_{0.36}W₁₈O₄₉. The crystalline phases in Al(W) were a metallic Al-W alloy, γ-Al₂O₃, and the blue oxide W₁₈O₄₉. Ta(W) contained crystalline α-TaH_{0.1}, δ-Ta₂O₅, hydrogen tungsten oxide, H_{0.23}WO₃, and blue WO_{3-x}. We detected metallic Cr, chromium tungsten(III) oxide, orthorhombic WO₃, and the tungsten blue oxide WO_{2.92} in the material prepared from Cr targets. We note that no iron-containing crystal phase was present in XRD data of Cr(W), indicating that all Fe in Cr(W) was amorphous. Pulsed laser synthesis of tungsten in aqueous AMT solution resulted in crystalline W metal, orthorhombic WO₃, and the tungsten blue

oxide $\text{WO}_{2.92}$.

The materials resulting from Mn, Fe, or Co targets were light brown, rusty red, or pink, respectively (Figure 1). The XRD pattern of Mn(W) was consistent with a mixture of manganese (hydr)oxides and manganese tungstate; no tungsten blue oxide was detectable. Fe(W) was predominantly X-ray amorphous, a small amount of crystalline magnetite was observed. XRD data of the material resulting from laser synthesis of Co in aqueous AMT solution showed the presence of crystalline cobalt tungstate, cubic WO_3 , and oxygen-deficient $\text{W}_{17}\text{O}_{47}$.

We prepared a series of Ni-W materials with systematically varied ratios of Ni and W precursors. The resulting materials had different relative proportions of Ni with respect to W, reflecting our precursor choices: the nanoparticles made from precursors with the highest ratio of Ni to W (Ni(W)-1) contained the highest amount of nickel and appeared white, whereas we found the lowest amount of nickel in a material that was synthesised from precursors with the lowest ratio of Ni to W (Ni(W)-4); that material was blue. The other Ni-W materials had Ni-to-W ratios and colours between the two extremes. We did not observe any crystalline tungsten blue oxide in XRD data of the white Ni-W material (14.3% Ni with respect to W, Ni(W)-1); its crystalline phases were nickel oxide hydroxide, $\text{Ni}_{1.94}\text{O}_2(\text{OH})_{0.81}$, nickel tungsten oxide hydroxide hydrate, $\text{Ni}_2(\text{Ni}(\text{OH})_6\text{W}_6\text{O}_{18}) \cdot 8 \text{H}_2\text{O}$, and tetragonal WO_3 . In contrast, our deep blue Ni-W material with 3.1% Ni with respect to W (Ni(W)-3) did contain a crystalline tungsten blue oxide, $\text{WO}_{2.83}$; orthorhombic and hexagonal WO_3 were also present.

In summary, the XRD data show that our pulsed-laser synthesis from metal targets in aqueous AMT solutions resulted in mixed-phase materials that contained the respective ad-metals and, depending on target metal, tungsten oxides with varying degrees of oxygen deficiency. Metastable polymorphs of WO_3 were also formed.

After we had established the elemental compositions and crystalline phases of our materials, we were interested in the oxidation states of the ad-metals, which we assessed by X-ray photoelectron spectroscopy (XPS, Figure S2 and Table S1). The ad-metal oxidation states at the surface were largely consistent with our XRD data, except that metallic Al was oxidised to Al^{3+} at the surface of Al(W), and we could not detect any surface chromium by XPS in Cr(W).

We observed in Al(W) a single peak in the Al 2s region with a central binding energy (CBE) of 118.9 eV, assignable to Al_2O_3 .^[34] We observed doublets with the expected branching ratios of 2:1 and corresponding satellite features in the 2p core-level regions of all first-row transition metals. In Cr(W), the CBE of the Fe 2p_{3/2} peak was 710.9 eV, consistent with Fe^{2+} or Fe^{3+} oxides or hydroxides; various iron oxides and oxyhydroxides, such as FeO, Fe_2O_3 , Fe_3O_4 , and $\text{Fe}(\text{O})\text{OH}$, have similar Fe core-level binding energies and spectral shapes.^[35] Similarly, XPS data of Fe(W) showed that the CBE of the Fe 2p_{3/2} peak was 711.0 eV, which we also assigned to various iron oxides and oxyhydroxides. The XP spectra of Mn(W) exhibited a CBE of 641.4 eV (Mn 2p_{3/2} peak), likewise attributable to various manganese oxides and oxyhydroxides.^[36] Co(W) had a Co 2p_{3/2} peak with a CBE of 780.0 eV, consistent with assignment to Co^{2+} .^[37] XPS data of the

Ni-W material with 14.3% Ni with respect to W (Ni(W)-1) showed three peaks in the Ni 2p_{3/2} region with CBEs of 855.7, 854.3 and 852.0 eV, which we attributed to $\text{Ni}(\text{OH})_2$ or $\text{Ni}^{3+}\text{-O}$, $\text{Ni}^{2+}\text{-O}$, and metallic Ni, respectively.^[38] We note that tripotential nickel has been reported in oxygen-deficient oxides.^[39] Cu(W) showed a single peak in the Cu 2p_{3/2} region, consistent with CuO .^[39] Analogous to our EDX results, we also detected aluminium in this Cu-based material; we found a single Al 2s peak with a CBE of 119.0 eV, which we assigned to Al_2O_3 .^[34] Zn(W) exhibited two peaks in the Zn 2p_{3/2} region with CBEs of 1024.1 and 1022.3 eV, consistent with assignment to ZnO and octahedrally coordinated Zn-O(H), respectively.^[40] We observed two peaks in the Ta 4d_{5/2} region of Ta(W), with CBEs of 230.6 and 227.1 eV, attributable to Ta_2O_5 and metallic Ta.^[41] And we obtained two peaks in the W 4d_{5/2} region of W(W), with CBEs of 248.0 and 244.0 eV attributable to WO_3 and metallic W.^[41b]

We collected scanning electron microscopy (SEM) images to visualise nanoparticle shapes and sizes (Figure 3). All particles provided high contrast as W has a high atomic number ($Z = 74$). For all materials, we observed aggregates of sub- μm -sized particles; aggregate formation is not surprising because we purified and dried our particles before re-suspending them without any surfactants in toluene for SEM sample preparation. Aggregation is natural for sub- μm -sized metal oxide particles and, importantly, is not an issue for use of the particles as solid-state photoanodes.

The SEM images (Figure 3) show that our particles had different morphologies. The material we synthesised from tungsten in water exhibited small, low-contrast structures, in accordance with reported laser-synthesised leaf-like WO_3 nanoplatelets.^[20] Laser synthesis of W metal in aqueous W^{6+} solution produced fused spheres. Koshizaki et al. have established that sub- μm -sized spheres of inorganic materials resulted from ultraviolet-laser based melting and fusion processes.^[19a] We obtained strongly aggregated nanosheets from laser synthesis of Mn metal in aqueous W^{6+} solution; such layered morphologies have been observed in various manganese oxides.^[42] All other materials except those made from Ni targets, exhibited less defined coagulated morphologies.

SEM images of our series of materials made from Ni targets revealed predominantly spherical morphologies. Interestingly materials with lower Ni-to-W ratios were formed as hollow spheres, whereas Ni(W)-1 (14.3% Ni with respect to W) consisted of solid spheres. To the best of our knowledge, this is the first time that laser-synthesised tungsten-based hollow nanospheres have been observed.

In related work, Koshizaki et al. reported hollow zirconia spheres that were fabricated by carbon-assisted selective laser heating in a liquid medium, using 532 nm pulses.^[43] Various hollow nanoparticles were accessible by infrared-laser syntheses.^[44] The mechanism for formation of hollow structures with millisecond 1064 nm pulses was studied in detail.^[44a] Briefly, the low power density of the long pulses led to metal nanodroplets (rather than vapour or plasma), whose surface reactions with liquid molecules produced partially oxidised core-shell nanoparticles. In systems with faster outward diffusion of metal core atoms and slower inward diffusion of oxide shell atoms (i.e.

where the nanoscale Kirkendall effect took place), the core-shell nanoparticles transformed into hollow morphologies.^[44a]

We used nanosecond 355 nm pulses to synthesise tungsten-based nanomaterials. In general, nanoparticle formation by pulsed-laser in liquids synthesis and concomitant morphology is a complex process that strongly depends on laser fluence, wavelength, pulse length, repetition rate, absorption cross section of the particles, and absorption properties of the resulting material.^[45]

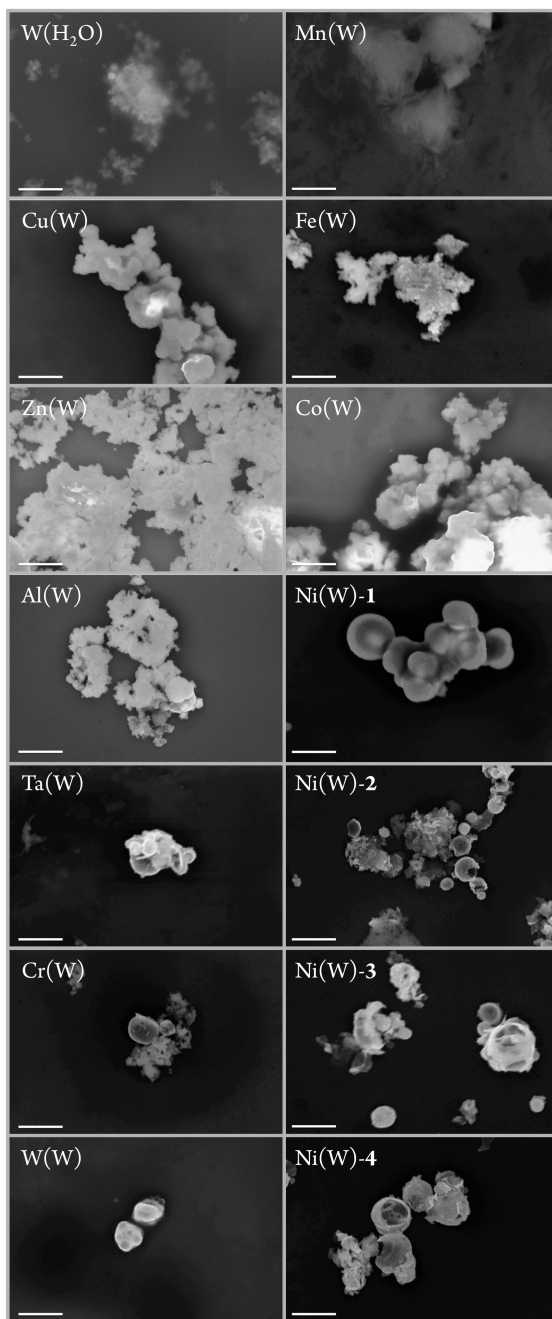


Figure 3. SEM images of laser-synthesised tungsten-based materials; see

Table 1 for nomenclature. All scale bars are 1 μm .

We collected optical spectra of our materials (Figure 4) in specular reflection mode. The y-axes in Figure 4 have arbitrary units because the optical path lengths were unknown. As expected for inorganic W^{6+} species, all materials exhibited strong absorptions in the ultraviolet. Except for particles made from copper in aqueous AMT solution, which appeared white, the spectra showed strong broad bands in the visible region; the colours of our materials are shown in Figure 1.

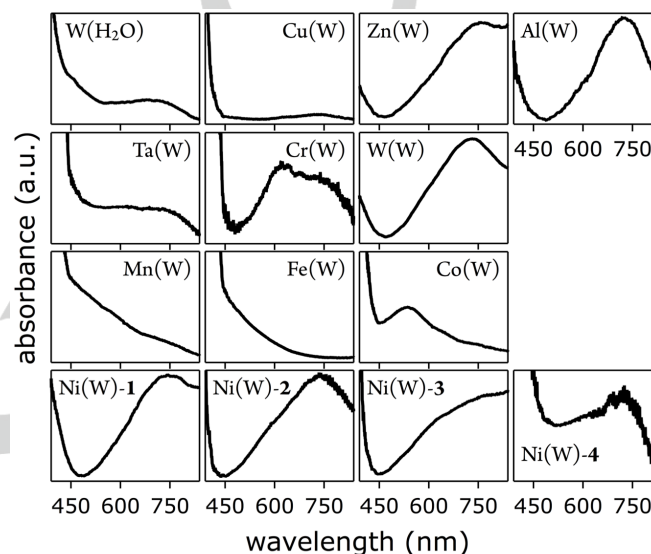


Figure 4. Optical spectra of laser-synthesised tungsten-based materials; see Table 1 for nomenclature.

We assessed photocurrent generation in strong aqueous acid. We chose HClO_4 because anion instead of water oxidation has been observed in other aqueous acids.^[10a] Assessment of photocurrent production of tungsten oxides in neat aqueous HClO_4 solution (without added hole acceptor) violates the principle of separating the challenges of light capture and catalysis (as in tandem photoelectrochemical devices, see Introduction) because oxidation reactions must occur at the surface of the light absorber. Unsurprisingly, photocorrosion of WO_3 in aqueous acid by peroxy-species formation has been reported.^[10e] The poor water oxidation activity of WO_3 can be overcome by use of a co-catalyst^[10c] or addition of a sacrificial hole-acceptor to the electrolyte.^[10a] We used 4-cyanopyridine N-oxide (CPO), which has been shown to be suitable for aqueous HClO_4 solutions.^[10a] For CPO with its fast oxidation kinetics, surface recombination of photogenerated holes is negligible, thus enabling determination of true photoanode performance.

We drop-cast our laser-synthesised tungsten-based materials from aqueous suspensions on fluorine-doped tin oxide (FTO) coated glass. The working electrodes were circular to prevent inhomogeneous electric fields across the active area. We deposited 50 μg nanoparticles on each electrode (0.159 cm^2

area). We did not optimize material layer thickness or adhesion to FTO. We measured the current densities of our materials as a function of applied bias with and without simulated sunlight illumination in 1.0 M (pH 0) aqueous HClO₄ with 0.20 M CPO electrolyte (Figure 5); we rapidly stirred the electrolyte to minimise mass transport effects. For comparison, we also prepared analogous electrodes with commercial WO₃.

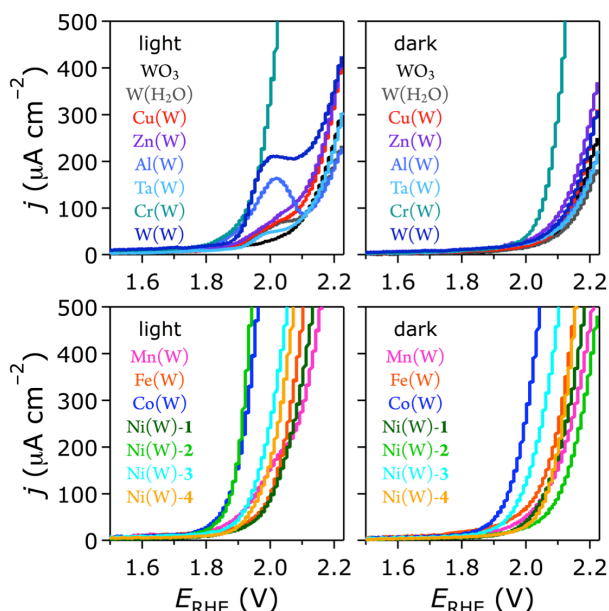


Figure 5. Current densities of laser-synthesised tungsten-based materials and commercial WO₃ with and without illumination in 1.0 M (pH 0) aqueous HClO₄ with 0.20 M CPO electrolyte; see Table 1 for nomenclature.

We found that, without illumination (denoted dark in Figure 5), all materials electrocatalytically oxidised CPO at applied potentials of >2 V vs RHE. We observed stark differences in CPO-oxidation activities across our laser-made particles in the dark: Co(W), Cr(W), and Ni(W)-3 performed best, followed by Fe(W), Ni(W)-4, Ni(W)-1, Mn(W), and Ni(W)-2, whereas materials synthesised from Cu, Zn, Al, Ta, and W targets were either inferior or only marginally better than commercial WO₃. Our results indicate that incorporation of a redox-active metal, whose higher oxidation states are accessible at moderate anodic potentials,^[27] is beneficial for high electrocatalytic activity, as has been suggested before.^[1]

Photocurrent onset potentials varied significantly between the materials (Figure 6). We found the best performance in mixed-metal tungsten oxides that contained ≤ 6.1 wt% nickel (with respect to W) or iron and chromium (Cr(W), which contained 1.1% Cr and 3.9% Fe with respect to W; Table 1). We obtained higher onset potentials in the other materials; W(W), Ni(W)-1, Cu(W), Ta(W), and Fe(W) were inferior to commercial WO₃.

We did not observe a correlation of onset potential with the colour of laser-made materials and thereby absorption of simulated sunlight (Figures 1 and 4). For example, the onset potential of Ni(W)-2 was cathodically shifted by 825 mV

compared to that of Fe(W), even though the overlap of red Fe(W) with the simulated solar spectrum was superior to that of pale greyish-blue Ni(W)-2. Likewise, photoelectrochemical performance was not a function of nanoparticle size (Figure 3). In general, light capture depends on the overlap of the absorber's optical spectrum (i.e. its bandgap) with the solar spectrum. The performance of photoelectrodes is not just governed by sunlight absorption, but band edge positions of the material in contact with the liquid electrolyte, material conductivity, carrier lifetimes, and charge recombination processes also matter; structure size critically affects the probability of a photogenerated carrier to reach the photoelectrode–electrolyte interface.^[9, 16] Since photocurrent generation of complex semiconductors depends on many factors,^[46] simple correlations are rarely found, especially when comparing different materials as in this work.

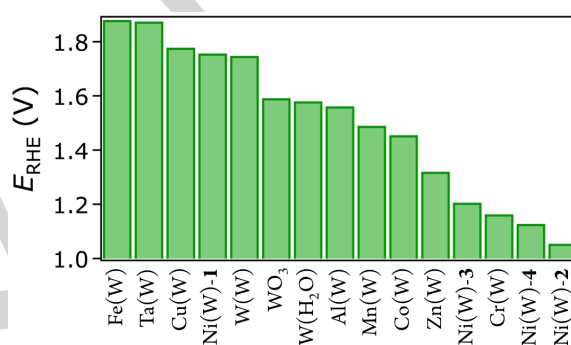


Figure 6. Photocurrent onset potentials vs RHE, measured in 1.0 M (pH 0) aqueous HClO₄ with 0.20 M CPO electrolyte; see Table 1 for nomenclature. The relative error is ±10%.

Relative proportions of the ad-metal to tungsten mattered for electrocatalytic and photocurrent generation activity, as evidenced by our series of Ni-W materials. Interestingly, relative nickel contents of best materials differed for electrocatalysis (in the dark) and photocurrent generation: Ni(W)-3, which contained approximately half of the nickel of Ni(W)-2 was the better electrocatalyst, whereas Ni(W)-2 was the superior photoanode material. This result confirms that separation of the challenges of light capture and catalysis enhances the prospects of discovering suitable materials for solar fuels generation.

Finally, we compared how much applied bias was needed to reach photocurrent densities of 0.1 or 0.25 mA cm⁻² (Figure 7). In these figures-of-merit, Ni(W)-2 again exhibited the best photoanode performance, followed by materials that we synthesised from Co and Cr targets, although Co(W) showed a fairly high onset potential. Since the main ad-metal content of Cr(W) was Fe (Table 1), we conclude that small amounts of nickel or iron most enhanced photocurrent generation of tungsten oxides.

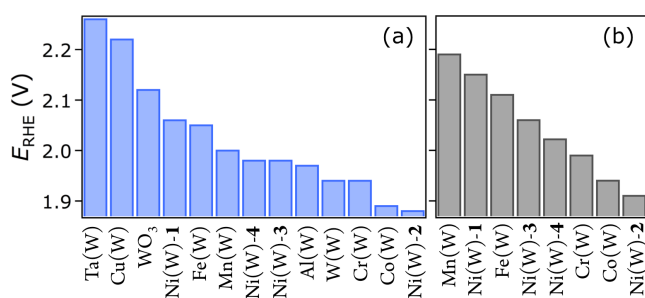


Figure 7. Potentials vs RHE needed to reach photocurrent densities of 0.10 (a) or 0.25 mA cm⁻² (b), measured in 1.0 M (pH 0) aqueous HClO₄ with 0.20 M CPO electrolyte; see Table 1 for nomenclature. The relative error is ±10%.

Our relative comparison of neat and mixed-metal tungsten oxide photoanodes showed that we were able to improve photoanode performance by incorporation of earth-abundant metals via pulsed-laser in liquids syntheses. Around 5% of iron or nickel proved especially beneficial. Both first-row transition metals have recently attracted much attention as water oxidation electrocatalysts in aqueous base.^[1] Here we demonstrated that the addition of iron or nickel to tungsten oxides enhanced photocurrent generation in strongly acidic aqueous electrolyte.

Conclusions

We prepared fourteen sub- μm -sized, differently coloured tungsten-oxide-based materials by ultraviolet pulsed-laser in liquids synthesis. Target metals were incorporated into materials upon synthesis from Al, Ta, or first-row transition metal targets in aqueous AMT solutions, whereas preparations from W targets in water or aqueous AMT solution resulted in materials that did not contain any ad-metals. We were able to access metastable polymorphs of WO₃ and tungsten oxides with varying degrees of oxygen deficiency. In a series of systematically varied Ni-to-W ratios, we found that Ni-W materials with $\leq 6\%$ Ni with respect to W formed hollow spheres.

Photoelectrochemistry data of our neat and mixed-metal tungsten oxide photoanode materials in strong aqueous acid revealed that materials with $\sim 5\%$ of iron or nickel performed best. We did not observe correlations of photocurrent generation with the colours or sizes of our laser-made materials. Relative proportions of the ad-metal to tungsten mattered for electrocatalytic and photocurrent generation activities.

Our pulsed-laser in liquids synthesis approach enabled us to rapidly produce a series of mixed-metal oxide light absorbers with different optical and photoelectrochemical properties for use in aqueous acid, systematically compare the resulting materials, and quickly identify which elemental compositions, crystal phases, and morphologies were most beneficial for enhanced photoanode performance.

Experimental Section

Materials and Methods. Laser synthesis was carried out in the Beckman Institute Laser Resource Center at the California Institute of Technology (Caltech). SEM images were collected at Caltech's GPS Division Analytical Facility. Photoelectrochemistry experiments were performed at the Molecular Materials Research Center (Beckman Institute at Caltech). All chemicals were used as received. Deionized water was obtained from a Barnstead Diamond Nanopure system and had a resistivity of ≥ 16 M Ω cm. Data analysis, unless otherwise noted, and graphing were performed with Igor Pro 6.37 (WaveMetrics, Inc.).

Materials Synthesis. Photoanode materials were prepared by pulsed-laser synthesis of metals in 10 mL water or aqueous solutions of ammonium metatungstate (AMT; Sigma-Aldrich, (NH₄)₆H₂W₁₂O₄₀ · xH₂O, puriss. p.a., $\geq 99.0\%$). Laser syntheses using metal powder or foil targets are described in more detail elsewhere.^[23-24, 25] Briefly, a 355 nm, 8 ns pulse laser beam, provided by the third harmonic of a 10 Hz Q-switched Nd:YAG laser (Spectra-Physics Quanta-Ray PRO-Series), was focused with a 100 mm focal length plano-convex quartz lens 1.0 mm below the surface of the liquid; for foil targets, the focus was at the metal disk. Each sample was irradiated at 150 mJ pulse⁻¹ for 60 min at room temperature in ambient air. The chemical precursors were W foil (Midwest Tungsten Service, 99.95%) in neat water, 2.0 g W powder (Alfa, >99%) in neat water or an aqueous solution of 3.0 g AMT, 2.0 g Cr powder (ESPI Metals, 99.7%), 0.75 g Mn powder (Sigma-Aldrich, $\geq 99.9\%$), or 1.0 g Fe powder (Alfa, 99+%) in aqueous solutions of 3.0 g AMT, 1.0 g Co powder (Sigma-Aldrich, $\geq 99.9\%$) in an aqueous solution of 5.0 g AMT, Cu foil (A.J. Oster, >95%), Zn foil (Alfa, 99.98%), or Al foil (Advent Research Materials Ltd., 99.5%) in aqueous solutions of 3.0 g AMT, or Ta foil (Eagle Alloys Corp., 99.9%) in an aqueous solution of 5.0 g AMT. Additionally, for a series of Ni-W materials with varying Ni-to-W proportions, we used 2.5 g, 1.8 g, or 0.9 g Ni powder (Alfa, 99.8%) in aqueous solutions of 3.0 g AMT, or 0.9 g Ni powder in an aqueous solution of 4.0 g AMT. After synthesis, material suspensions were separated from target metals by gravity or a rare-earth magnet, and solid particles were obtained by centrifugation and washing with water until the supernatant was free of any AMT absorption. We then washed the materials twice with acetone (EMD, OmniSolv®) and dried them under vacuum.

Physical Characterisation. We obtained electron microscopy images with a Zeiss LEO 1550VP Field-Emission SEM, operated at 5 kV and a working distance of 9.4 mm. Particles were drop-cast on 5 mm × 5 mm silicon chips (Ted Pella) from material suspensions in toluene (Sigma-Aldrich, >99.9%; ~ 0.1 mg mL⁻¹) that were sonicated for 5 sec (Branson 3200); the samples were dried overnight in ambient air at room temperature. The silicon chips were attached to SEM stubs with carbon tape. We employed energy-dispersive X-ray (EDX) spectroscopy to identify chemical elements in the laser-synthesised particles. We used an Oxford X-Max SDD X-ray Energy Dispersive Spectrometer, which allowed quantitative elemental analysis with a relative accuracy of better than 2% and detection limit of better than 0.5%. We acquired EDX histograms on three different spots on each material and averaged the measured compositions. EDX data acquisition and analysis was performed with the AZtec software package.

We took XPS data with a Surface Science Instruments M-probe surface spectrometer, using monochromatic Al K α radiation (1486.6 eV) and a vacuum chamber pressure of $<5 \times 10^{-9}$ Torr. We attached dry materials to double-sided adhesive carbon tape (Electron Microscopy Sciences) on XPS stubs. Depending on the elemental composition of the materials, as determined by EDX, we collected high-resolution spectra in the Al 2s, Cr 2p, Mn 2p, Fe 2p, Co 2p, Ni 2p, Cu 2p, Zn 2p, Ta 4d, or W 4d regions.

We obtained binding energies from Gaussian-Lorentzian peak fits after Shirley background subtraction^[47] and referenced them to the C 1s peak arising from adventitious carbon, taken to have a binding energy of 284.8 eV.^[48] We performed XPS data analysis with CasaXPS (Version 2.3.16 PR 1.6).

We collected powder XRD data with a Bruker D2 PHASER diffractometer, using monochromatic Cu K α radiation (1.5418 Å; tube power 30 kV, 10 mA) and 0.1° divergence, 2.5° Soller, and 0.6 mm detector slits; the instrument also had a 3-mm secondary anti-scatter screen and a Lynxeye detector. The resolution was 0.020° in 2θ , and the counting time was 3.0 seconds per step. We mounted solid samples with Vaseline (X-Alliance GmbH) on a zero-diffraction silicon plate (MTI Corporation). Background subtraction, and XRD pattern matching was performed with the Bruker DIFFRAC.SUITE software coupled to the International Centre for Diffraction Data powder diffraction file database (ICDD, PDF-2 Release 2012).

We analysed aluminium content in the copper foil with an Agilent Technologies 8800 ICP-MS Triple Quad instrument, which was calibrated using Cu and Al concentration standards. We dissolved 26 mg copper foil in concentrated trace-metal-free 70% nitric acid and diluted the solution with 2% nitric acid to below 1 ppm before injection into the instrument; solutions were prepared in plastic vials to prevent accidental trace-metal contaminations by contact with glassware.

We measured optical spectra in specular reflection mode with an Oriel Nic-Plan™ microscope that was equipped with an EG&G Princeton Applied Research Model 1235 digital triple grating spectrograph and an EG&G PARC Model 1452-NIR detector. Small amounts of the dried laser-synthesised materials were placed on quartz windows (GM Associates, Inc.) and positioned under a 10X magnification objective. We used an aluminium mirror or a piece of aluminium foil as reflection standards and acquired 10 scans for each sample.

Photoanode Preparation. Photoanodes were prepared by modifying a procedure reported elsewhere.^[46] We used FTO-glass substrates purchased from Hartford Glass Co. (TEC 15, surface resistivity ~15 Ω /sq). FTO-glass slides were cut into ~1.0 cm \times 2.5 cm pieces and (i) rinsed with water and patted dry with a Kimwipe, (ii) rinsed with a 1/1 (v/v) mixture of acetone and methanol (both EMD, HPLC grade) and patted dry with a Kimwipe, (iii) surface-etched by submerging for 3 seconds in concentrated hydrochloric acid (Macron), rinsed with water, and patted dry with a Kimwipe. We placed two 4.5-mm diameter metal disks on the FTO, one at a short edge (to attach a wire lead), and the other centred with respect to the short edge and ~1.5 cm away from the first disk to create a defined area for sample deposition and photoelectrochemical testing. The two metal disks acted as masks, and we covered all FTO around these masks with black high-temperature spray paint (McMaster-Carr). After the spray paint had dried, we firmly attached a silver-coated copper wire with silver paint (SPI, high purity) to the bare FTO at the edge. For mechanical stability the wire was run inside a glass tube, whose end and all exposed conducting parts were sealed with an epoxy adhesive (Loctite Hysol 9460). We confirmed that the paint and epoxy were stable in our electrolyte.

We drop-cast the laser-synthesised particles or commercial WO₃ (Strem, 99.5%) powder onto FTO from 2.5 mg mL⁻¹ aqueous suspensions. We used a high precision balance (Sartorius CPA225D) to weigh the materials. After sonicating each suspension for 30 min, 20 μ L were placed on a bare circular FTO spot, and the photoanode layers were dried overnight in ambient air. We placed 10 μ L 0.125 mg mL⁻¹ aqueous Nafion solution (Sigma-Aldrich, 5 wt % Nafion® 117 solution in a mixture of lower aliphatic alcohols and water, diluted with water to obtain an

active material to Nafion mass ratio of 40/1) on top of the particle layer and dried the electrodes for 10 min at 60°C under a heat lamp. Each electrode had a material loading of 50 μ g and a circular active area of 0.159 cm². Current densities were calculated from measured currents by normalization to the geometric electrode area.

Photoelectrochemical Characterisation. Linear sweep voltammograms were collected with a Gamry Reference 600 potentiostat at room temperature and in ambient air (scan rate 10 mV s⁻¹). Electrochemical experiments were carried out in a standard Pyrex three-electrode single-compartment electrochemical cell equipped with a flat quartz window for illumination. The electrolyte was 1.0 M (pH 0) aqueous HClO₄ (J.T.Baker, 60-62%, diluted to 1.0 M; pH 0.0, measured with a VWR model SympHony SB70P pH meter, equipped with a Thermo Scientific model Orion 9102BNWP electrode) with added 0.20 M 4-cyanopyridine N-oxide (CPO, TCI America, >98%; pH 0.04). We collected current vs. potential data while the liquid was rapidly stirred, to minimize mass transport effects; the data were not corrected for any uncompensated resistance losses because conductivities of photoactive materials are dependent on the illumination. We used a curled Pt wire (Surepure Chemetals, LLC, 99.95%) counter electrode and a calibrated Ag/AgCl (3.0 M NaCl) reference electrode (Bioanalytical Systems, Inc., measured to be +0.212 V vs the normal hydrogen electrode; the calibration method has been described elsewhere).^[23] All potentials reported here are relative to the reversible hydrogen electrode (RHE), calculated using the Nernstian relation $E_{\text{RHE}} = E_{\text{Ag/AgCl}} + 0.0591 \cdot \text{pH} + 0.212 \text{ V}$.

We measured photoanode performance under 1 sun AM 1.5G simulated sunlight, which was supplied by an Oriel 96000 solar simulator consisting of a 150 W xenon arc lamp and Oriel 81094 filter (the spectrum has been reported elsewhere).^[46] The incident photon flux was equivalent to 1 sun illumination, as verified by a calibrated Si photodiode (Thorlabs). We used three electrodes per material and observed good reproducibility. We collected photoelectrochemistry data with and without illumination; photocurrents were calculated as the difference of currents measured with and without illumination. We determined onset potentials by fitting lines to photocurrent data in the vicinity of photocurrent onset and calculating intersections of the tangents between the baseline and the signal currents.

Acknowledgements

We thank George Rossman for help with optical spectroscopy, Chi Ma for help with SEM (both Division of Geological and Planetary Sciences Caltech), and Nathan Dalleska (Environmental Analysis Center at Caltech) for help with ICP-MS. We performed research in the Laser Resource Center and the Molecular Materials Research Center of the Beckman Institute of the California Institute of Technology. The NSF CCI Solar Fuels Program (CHE-1305124) and the Arnold and Mabel Beckman Foundation supported this work.

Keywords: pulsed-laser synthesis • tungsten oxide • mixed-metal oxides • photoanodes • solar water splitting

References

- [1] B. M. Hunter, H. B. Gray, A. M. Müller *Chem. Rev.* **2016**, *116*, 14120-14136.

- [2] a) N. S. Lewis, D. G. Nocera *Proc. Natl. Acad. Sci. U. S. A.* **2006**, *103*, 15729-15735; b) H. B. Gray *Nature Chem.* **2009**, *1*, 7-7; c) T. R. Cook, D. K. Dogutan, S. Y. Reece, Y. Surendranath, T. S. Teets, D. G. Nocera *Chem. Rev.* **2010**, *110*, 6474-6502.
- [3] a) O. Khaselev, J. A. Turner *Science.* **1998**, *280*, 425-427; b) M. G. Walter, E. L. Warren, J. R. McKone, S. W. Boettcher, Q. Mi, E. A. Santori, N. S. Lewis *Chem. Rev.* **2010**, *110*, 6446-6473.
- [4] S. W. Boettcher, E. L. Warren, M. C. Putnam, E. A. Santori, D. Turner-Evans, M. D. Kelzenberg, M. G. Walter, J. R. McKone, B. S. Brunschwig, H. A. Atwater, N. S. Lewis *J. Am. Chem. Soc.* **2011**, *133*, 1216-1219.
- [5] A. Heller, B. Miller, H. Lewerenz, K. Bachmann *J. Am. Chem. Soc.* **1980**, *102*, 6555-6556.
- [6] J. R. McKone, A. P. Pieterick, H. B. Gray, N. S. Lewis *J. Am. Chem. Soc.* **2012**, *135*, 223-231.
- [7] a) K. Sivula *J. Phys. Chem. Lett.* **2013**, *4*, 1624-1633; b) L. Trotochaud, T. J. Mills, S. W. Boettcher *J. Phys. Chem. Lett.* **2013**, *4*, 931-935.
- [8] B. A. Pinaud, J. D. Benck, L. C. Seitz, A. J. Forman, Z. Chen, T. G. Deutsch, B. D. James, K. N. Baum, G. N. Baum, S. Ardo, H. Wang, E. Miller, T. F. Jaramillo *Energy Environ. Sci.* **2013**, *6*, 1983-2002.
- [9] M. S. Prévot, K. Sivula *J. Phys. Chem. C.* **2013**, *117*, 17879-17893.
- [10] a) Q. Mi, A. Zhanidarova, B. S. Brunschwig, H. B. Gray, N. S. Lewis *Energy Environ. Sci.* **2012**, *5*, 5694-5700; b) Y. Miseki, K. Sayama *RSC Adv.* **2014**, *4*, 8308-8316; c) J. M. Spurgeon, J. M. Velazquez, M. T. McDowell *Phys. Chem. Chem. Phys.* **2014**, *16*, 3623-3631; d) J. C. Hill, K.-S. Choi *J. Phys. Chem. C.* **2012**, *116*, 7612-7620; e) B. D. Alexander, P. J. Kulesza, I. Rutkowska, R. Solarska, J. Augustynski *J. Mater. Chem.* **2008**, *18*, 2298-2303; f) R. Liu, Y. Lin, L. Y. Chou, S. W. Sheehan, W. He, F. Zhang, H. J. Hou, D. Wang *Angew. Chem.* **2011**, *123*, 519-522.
- [11] C. G. Granqvist *Sol. Energy Mater. Sol. Cells.* **2000**, *60*, 201-262.
- [12] a) A. Kudo, Y. Miseki *Chem. Soc. Rev.* **2009**, *38*, 253-278; b) C. Di Valentin, G. Pacchioni *Acc. Chem. Res.* **2014**, *47*, 3233-3241.
- [13] a) Q. Mi, Y. Ping, Y. Li, B. Cao, B. S. Brunschwig, P. G. Khalifah, G. A. Galli, H. B. Gray, N. S. Lewis *J. Am. Chem. Soc.* **2012**, *134*, 18318-18324; b) Y. Ping, Y. Li, F. Gygi, G. Galli *Chem. Mater.* **2012**, *24*, 4252-4260.
- [14] M. Ma, K. Zhang, P. Li, M. S. Jung, M. J. Jeong, J. H. Park *Angew. Chem.* **2016**, *128*, 11998-12002.
- [15] Y. Ping, G. Galli *J. Phys. Chem. C.* **2014**, *118*, 6019-6028.
- [16] T. A. Pham, Y. Ping, G. Galli *Nat. Mater.* **2017**, advance online publication.
- [17] M. Gerosa, C. Di Valentin, G. Onida, C. E. Bottani, G. Pacchioni *J. Phys. Chem. C.* **2016**, *120*, 11716-11726.
- [18] A. Fojtik, A. Henglein *Ber. Bunsen-Ges. Phys. Chem.* **1993**, *97*, 252-254.
- [19] a) Y. Ishikawa, Y. Shimizu, T. Sasaki, N. Koshizaki *Appl. Phys. Lett.* **2007**, *91*, 161110; b) G. W. Yang *Prog. Mater. Sci.* **2007**, *52*, 648-698; c) A. V. Kabashin *Laser Phys.* **2009**, *19*, 1136-1141; d) Y. Ishikawa, Q. Feng, N. Koshizaki *Appl. Phys. A.* **2010**, *99*, 797-803; e) R. Sibirian, J. Nakamura *J. Phys. Chem. C.* **2012**, *116*, 22947-22953; f) H. Zeng, X. W. Du, S. C. Singh, S. A. Kulinich, S. Yang, J. He, W. Cai *Adv. Funct. Mater.* **2012**, *22*, 1333-1353; g) S. Barcikowski, G. Compagnini *Phys. Chem. Chem. Phys.* **2013**, *15*, 3022-3026; h) Y. Onodera, T. Nunokawa, O. Odawara, H. Wada *J. Lumin.* **2013**, *137*, 220-224; i) R. Sibirian, T. Kondo, J. Nakamura *J. Phys. Chem. C.* **2013**, *117*, 3635-3645; j) V. Amendola, S. Scaramuzza, L. Litt, M. Meneghetti, G. Zuccolotto, A. Rosato, E. Nicolato, P. Marzola, G. Fracasso, C. Anselmi, M. Pinto, M. Colombatti *Small.* **2014**, *10*, 2476-2486; k) M. Lau, S. Barcikowski *Appl. Surf. Sci.* **2015**, *348*, 22-29; l) S. Scaramuzza, S. Agnoli, V. Amendola *Phys. Chem. Chem. Phys.* **2015**, *17*, 28076-28087; m) H. Wang, O. Odawara, H. Wada *Sci. Rep.* **2016**, *6*, 20507.
- [20] H. Zhang, G. Duan, Y. Li, X. Xu, Z. Dai, W. Cai *Cryst. Growth Des.* **2012**, *12*, 2646-2652.
- [21] H. Zhang, Y. Li, G. Duan, G. Liu, W. Cai *CrystEngComm.* **2014**, *16*, 2491-2498.
- [22] S. Wang, K. Dou, Y. Zou, Y. Dong, J. Li, D. Ju, H. Zeng *J. Colloid Interface Sci.*
- [23] J. D. Blakemore, H. B. Gray, J. R. Winkler, A. M. Müller *ACS Catal.* **2013**, *3*, 2497-2500.
- [24] a) B. M. Hunter, J. D. Blakemore, M. Deimund, H. B. Gray, J. R. Winkler, A. M. Müller *J. Am. Chem. Soc.* **2014**, *136*, 13118-13121; b) B. M. Hunter, W. Hieringer, J. R. Winkler, H. B. Gray, A. M. Müller *Energy Environ. Sci.* **2016**, *9*, 1734-1743.
- [25] C. W. Roske, J. W. Lefler, A. M. Müller *J. Colloid Interface Sci.* **2017**, *489*, 68-75.
- [26] J. Y. C. Chen, J. T. Miller, J. B. Gerken, S. S. Stahl *Energy Environ. Sci.* **2014**, *7*, 1382-1386.
- [27] M. Pourbaix, *Atlas of Electrochemical Equilibria in Aqueous Solutions*, Pergamon Press, New York, **1966**.
- [28] P. Blandin, K. A. Maximova, M. B. Gongalsky, J. F. Sanchez-Royo, V. S. Chirvony, M. Sentis, V. Y. Timoshenko, A. V. Kabashin *J. Mater. Chem. B.* **2013**, *1*, 2489-2495.
- [29] We stated mass of ammonium metatungstate (AMT) instead of molarity because the molecular weight of AMT is unknown; AMT contains multiple water molecules.
- [30] a) H. J. Lunk, B. Ziemer, M. Salmen, D. Heidemann *Int. J. Refract. Met. Hard Mater.* **1994**, *12*, 17-26; b) E. Lassner, W.-D. Schubert *Int. J. Refract. Met. Hard Mater.* **1995**, *13*, 111-117.
- [31] J. L. Walter, K. A. Lou *J. Mater. Sci.* **1989**, *24*, 3577-3587.
- [32] M. Kim, B. Y. Lee, H. C. Ham, J. Han, S. W. Nam, H.-s. Lee, J. H. Park, S. Choi, Y. Shin *J. Supercrit. Fluids.* **2016**, *111*, 8-13.
- [33] L. Trotochaud, S. L. Young, J. K. Ranney, S. W. Boettcher *J. Am. Chem. Soc.* **2014**, *136*, 6744-6753.
- [34] Y. Okamoto, T. Imanaka, S. Teranishi *J. Catal.* **1980**, *65*, 448-460.
- [35] W. Temesghen, P. Sherwood *Anal. Bioanal. Chem.* **2002**, *373*, 601-608.
- [36] M. C. Biesinger, B. P. Payne, A. P. Grosvenor, L. W. Lau, A. R. Gerson, R. S. C. Smart *Appl. Surf. Sci.* **2011**, *257*, 2717-2730.
- [37] *NIST X-ray Photoelectron Spectroscopy Database*, X-ray Photoelectron Spectroscopy Database 20, Version 4.1 (National Institute of Standards and Technology, Gaithersburg, 2012); <http://srdata.nist.gov/xps/>.
- [38] a) S. Uhlenbrock, C. Scharfschwerdt, M. Neumann, G. Illing, H.-J. Freund *J. Phys.: Condens. Matter.* **1992**, *4*, 7973; b) A. N. Mansour, C. A. Melendres *Surf. Sci. Spectra.* **1994**, *3*, 247-254.
- [39] G. Ertl, R. Hierl, H. Knözinger, N. Thiele, H. Urbach *Appl. Surf. Sci.* **1980**, *5*, 49-64.
- [40] a) N. J. Nicholas, G. V. Franks, W. A. Ducker *CrystEngComm.* **2012**, *14*, 1232-1240; b) S. Bera, A. Prince, S. Velmurugan, P. Raghavan, R. Gopalan, G. Panneerselvam, S. Narasimhan *J. Mater. Sci.* **2001**, *36*, 5379-5384.
- [41] a) G. McGuire, G. K. Schweitzer, T. A. Carlson *Inorg. Chem.* **1973**, *12*, 2450-2453; b) S. Kerber, J. Bruckner, K. Wozniak, S. Seal, S. Hardcastle, T. Barr *J. Vac. Sci. Technol., A.* **1996**, *14*, 1314-1320.
- [42] a) B. A. Pinaud, Z. Chen, D. N. Abram, T. F. Jaramillo *J. Phys. Chem. C.* **2011**, *115*, 11830-11838; b) M. Wiechen, I. Zaharieva, H. Dau, P. Kurz *Chem. Sci.* **2012**, *3*, 2330-2339; c) M. Huynh, C. Shi, S. J. L. Billinge, D. G. Nocera *J. Am. Chem. Soc.* **2015**, *137*, 14887-14904.
- [43] X. Li, Y. Shimizu, A. Pyatenko, H. Wang, N. Koshizaki *Nanotechnology.* **2012**, *23*, 115602.
- [44] a) K. Niu, J. Yang, S. Kulinich, J. Sun, H. Li, X. Du *J. Am. Chem. Soc.* **2010**, *132*, 9814-9819; b) G. Viau, V. Collière, L.-M. Lacroix, G. Shafeev *Chem. Phys. Lett.* **2011**, *501*, 419-422; c) P. Kuzmin, G. Shafeev, G. Viau, B. Warot-Fonrose, M. Barberoglou, E. Stratakis, C. Fotakis *Appl. Surf. Sci.* **2012**, *258*, 9283-9287; d) Z. Yan, D. B. Chrisey *J. Photochem. Photobiol. C: Photochem. Rev.* **2012**, *13*, 204-223; e) H. Desarkar, P. Kumbhakar, A. Mitra *Laser Phys. Lett.* **2013**, *10*, 055903; f) J. Santillán, F. Videla, M. F. van Raap, D. Muraca, L. Scaffardi, D. Schinca *J. Phys. D: Appl. Phys.* **2013**, *46*, 435301.
- [45] V. Amendola, M. Meneghetti *Phys. Chem. Chem. Phys.* **2013**, *15*, 3027-3046.

-
- [46] T. S. Sinclair, B. M. Hunter, J. R. Winkler, H. B. Gray, A. M. Müller *Mater. Horiz.* **2015**, *2*, 330-337.
- [47] D. A. Shirley *Phys. Rev. B.* **1972**, *5*, 4709-4714.
- [48] T. L. Barr, S. Seal *J. Vac. Sci. Technol. A.* **1995**, *13*, 1239-1246.

WILEY-VCH

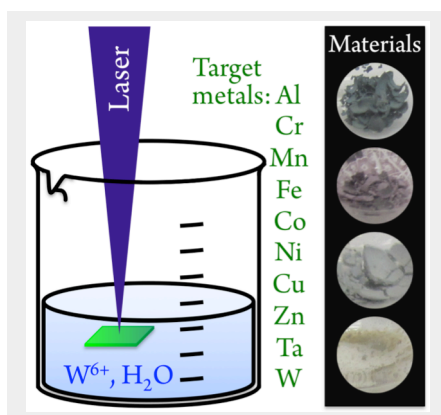
Accepted Manuscript

Entry for the Table of Contents (Please choose one layout)

Layout 1:

ARTICLE

We prepared a series of sub- μm -sized, differently coloured mixed-metal oxide light absorbers by ultraviolet pulsed-laser in liquids synthesis. Assessment of their photoelectrochemical properties in strong aqueous acid allowed us to quickly identify which elemental compositions, crystal phases, and morphologies were most beneficial for enhanced photoanode performance.



Carl M. Blumenfeld, Marcus Lau, Jay R. Winkler, Harry B. Gray, Astrid M. Müller*

Page No. – Page No.

**Mixed-Metal Tungsten Oxide
Photoanode Materials Made by
Pulsed-Laser in Liquids Synthesis**